ACS APPLIED POLYMER MATERIALS

pubs.acs.org/acsapm Article

Emergence of Structural Phosphorescence in Free-Standing, Laterally Organized Polymer Nanofiber Membranes

Mirella Wawryszyn, Robin Wilhelm, John Kim, Xiaoyang Zhong, Jeffery E. Raymond, Richard Thelen, Vanessa Trouillet, Matthias Schwotzer, Stefan Bräse, Do Hoon Kim, Nicholas L. Abbott, and Joerg Lahann*

Cite This: ACS Appl. Polym. Mater. 2023, 5, 1670−1680 Read Online

ACCESS | Metrics & More | Article Recommendations | Supporting Information

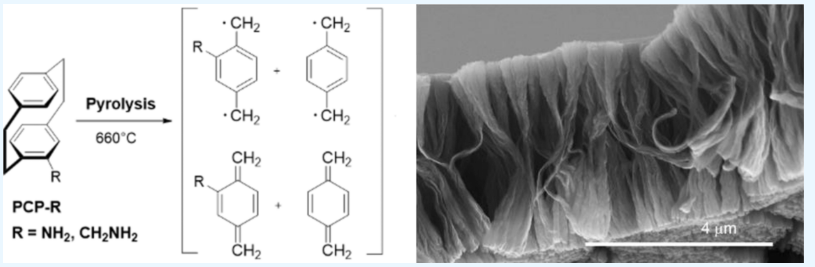

ABSTRACT: In the past decade, the phosphorescence of metal-free confined polymer structures has generated interest in optoelectronics due to their sustainability, low toxicity, and deployment in sensing applications. Herein, a free-standing array of laterally organized nanofibers was prepared via templated chemical vapor deposition polymerization into a liquid crystalline (LC) phase, and their optical properties were compared to compositionally identical films. The fibers converge into laterally aligned membranes that maintain a high internal order despite the surfaces of the membranes remaining uniform and closed. The membranes consisted of hourglass-shaped nanofibers with features in the micro- and nanometer regime. Free-standing nanofiber membranes differ from polymer films of equivalent chemical composition in several key features: (1) Anisotropic growth of polymer nanofibers with constraint and compliance to an LC template, (2) a high surface-to-volume ratio, and (3) the occurrence of a long-lived emission in the blue region, which persists for multiple seconds after excitation. This study constitutes the first report of long-lived emission from solid-state poly(*p*-xylylenes) nanofibers. Prospective applications of morphologically controlled polymer arrays with structural luminescence include organic sensors and optoelectronic devices.

KEYWORDS: *liquid crystal (LC) templated chemical vapor deposition (CVD), 3D laterally organized free-standing nanofiber membranes, surface enhancement, room-temperature luminescence, phosphorescence*

INTRODUCTION

The photophysical response of solid-state organic compounds that exhibit luminescence can be utilized in a range of different optoelectronic or bioimaging applications.[1,2] The structural emergence of phosphorescence at room temperature typically coincides with exceptional conformational order, unique molecular packing, high rigidity, and/or global morphology of suitable chemical composition.[2−4] Generally, this emergent response is due to triplet interconversion ($S_0 \rightarrow S_n \rightarrow T_n$); the structural components of this change to a phosphorescent state include the induction of strong $\pi-\pi$ interactions, dipole−electron interactions (such as $\pm\delta-\pi$ or $\pm\delta$−lone pair), dipole−dipole interactions, and/or the introduction of delocalized/trapped excited states. This effect is further enhanced if the chemical or structural composition stabilizes an excited triplet state (after intersystem crossing), generating long-lived emission.[1,5−7]

The origin of emission due to structural properties in organic nanostructures can be varied.[8] Examples include edge or core luminescence due to unique boundary conditions[9] and various types of $\pi-\pi$ interactions relative to the transition dipole of the effective molecular orbital of a subunit.[10] However, the emergence of emission from long-lived states in closely interacting systems typically occurs due to the presence of a delocalized exciton.[11] Delocalized excitons may be a trapped singlet that has a very long-lived relaxation,[12] a trapped singlet that gives an otherwise dark triplet state a chance to populate,[13] an increase in the overlap of the singlet

Received: August 24, 2022
Accepted: January 25, 2023
Published: February 9, 2023

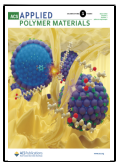

and triplet,[14] or something more exotic,[15] such as the effects observed in natural light-harvesting systems.[16−19]

In the case of nanoscale solid-state polymeric structures, three mechanisms tend to dominate if phosphorescence emerges in the nanostructure but is not observed in the unstructured bulk polymer.[8,11] In one mechanism, conformational changes in the backbone may lead to ordering or symmetry breaking that does not occur in the bulk materials.[10] This may result in the production of delocalized excited states that possess "fuzzy" selection rules (ordering), leading to enhanced interconversion to otherwise dark triplet states.[10,15] Conversely, symmetry breaking may lead to trapped excitons that allow for an otherwise slow and unobserved interconversion to occur based simply on superior kinetic conditions.[15] The second mechanism is one in which the nanostructure dictates interchain interactions, similar to aggregation-induced emission, which may induce the same two effects: delocalization or trapping.[12] In this case, the effect may be regional (arising at the surface, in the core, or at the ends of structures).[9,12] The third mechanism is exclusive to highly ordered and very small structures, where defects in the structure function similarly to defects or doping in semiconductor quantum dots.[8,12,20,21] The defects give rise to the long-lived states by functioning as quantum wells that trap excitons outside of the emergent band structure. In most polymeric systems where crystalline "quantum boxes" are not present, such as nanofibers and nanorods, the mechanism for the emergence of phosphorescent character is a blend of both the first and second mechanism: both intrachain and interchain electronic interactions are induced by the nanostructure of the system, giving rise to emergent optical phenomena.

Though the mechanisms for organic phosphorescence in nanostructures may be convolved, much of the interest in these synthetic systems is inspired by naturally occurring structures where both structural and chemical optoelectronic effects are in play.[22] Despite attempts to adapt some of these long-lived emissive systems to luminescent or energy conversion applications, the emergence of structurally induced phosphorescence has not been fully explored.[22] From a synthetic perspective, solid-state room temperature phosphorescence can be achieved with a suitable set of structural, regional, and chemical properties, leading to changes in the emissive properties.[2,9,23−25] One strategy that is inspired by nature arises from the use of ordered support systems, specifically the use of liquid crystals. Liquid crystals (LCs) can be utilized to help guide, grow, or position materials to generate nano- and microscale order. This, in turn, can lead to structurally induced changes in luminescent properties.[4,26]

Herein, we report polymer membranes with high lateral organization via the implementation of free-standing LC films, in which the LC film serves as a template and is later removed. The resultant three-dimensional structures possess structurally emergent phosphorescence that is not observed in bulk films of identical chemical compositions.[3,9,27,28] Preliminary work by our team has centered around using LCs to template aligned nano- and micro-structured nanofiber arrays on supportive substrates.[29,30] These works have used LC templates during chemical vapor deposition (CVD) polymerization to produce morphologically controlled, high-molecular-weight poly(*p*-xylylene)-based nanofibers.[29,31]

MATERIALS AND METHODS

Materials and Sample Preparation. 4-(Amino)[2.2]-paracyclophane (PCP-NH_2) and 4-(aminomethyl)[2.2]-paracyclophane (PCP-CH_2NH_2) precursors were synthesized as described elsewhere.[32,33] The LC E7 (nematic mixture of cyanobiphenyl and cyanoterphenol components) was purchased from Merck. The rectangular transmission electron microscopy (TEM) copper grids (1.00 cm × 0.40 cm × 15.00 μm, type AGB7753) with a pore width of 200 μm and a bar width of 40 μm were bought from Agar Scientific. The 30% hydrogen peroxide solution, concentrated sulfuric acid, ethanol, and isopropanol were purchased from Merck.

Before LC loading, the copper grids were exposed to oxygen plasma (Pie Scientific Teveo) or sonicated for 10 mins in a piranha solution (30% hydrogen peroxide and concentrated sulfuric acid, 7:1) and rinsed with deionized water, ethanol, and isopropanol. Subsequently, the TEM grids were mounted onto 1.40 cm × 0.80 cm × 600 μm rectangular stainless-steel frames (Microphoto, Inc.). 2 μL of E7 was dispensed with a glass capillary (Marienfeld Superior, prod. No.: 2930203) and suspended in the free-standing TEM-grid pores. Afterward, the construct was heated to 35 °C and slowly cooled down to room temperature, allowing the LCs to air-align. The constructs were placed inside the CVD chamber and utilized immediately for CVD polymerization. The system was pumped down in 20% increments and purged with 20 sccm Ar-flow until a system pressure of 0.2 mbar (+/−0.05 mbar) was reached. After stabilization of the CVD pressure, 10−20 mg of the respective precursors (PCP-NH_2 or PCP-Me-NH_2) was sublimed and then pyrolyzed into the reactive quinodimethane intermediate at 660 °C. Recombination of the reactive gas then led to the formation of 4-(amino)- or 4-(aminomethyl)-substituted poly-*para*-xylylene inside the TEM-grid pores. The setpoint for the stage temperature was set to between −10 °C and 0 °C. A thermal probe was used to determine the relationship between this setpoint of the stage and the temperature of the substrate in this system, with the actual substrate temperature calculated to be between 15 and 20 °C. To prevent preferential deposition on the chamber surface, a heating mantle was utilized to increase the temperature of the chamber (80 °C mantle setpoint).

After CVD polymerization, the samples were placed into a glass petri dish filled with ethanol (first) and isopropanol (second) for 10 min in order to remove the remaining LC film after CVD polymerization. The samples were then dried under atmospheric conditions prior to chemical, topographical, and photophysical analysis. Some samples were retained in which the LC was not removed, as noted in later analysis.

Imaging. *Vertical Scanning Interferometry.* Information about film geometry and surface character was obtained with a Bruker Contour GT-K0 device and analyzed with Vision 64 software (Bruker). These measurements were carried out on the TEM grids that possessed the LC, LC with film, and the films after LC removal. Briefly, the Bruker 3-D optical microscope is a combination of phase-shift imaging and white light interferometry utilizing the wavelength-dependent diffraction as height information with high vertical (<0.3 nm) and lateral (<380 nm, Sparrow Criterion) resolution and broadly categorized as vertical scanning interferometry (VSI). Moreover, the option of taking measurements with a green light source is given. Limitations for the height measurement range without generating phase jumps, when using phase-shift imaging solely, is $\lambda/4$ (ca. 100 nm for green light). Magnifications were obtained with either a 5× or a 50× objective in combination with either a 1× or 0.55× field of view (FOV) lens, giving the following $x-y$ (lateral) FOVs: 5×/0.55×, FOV 1.74 × 1.30 mm; 5×/1×, FOV 96 × 72 μm; 50×/1.0×, FOV 960 × 720 μm. Depth profiles were obtained with a back scan that was set to 5 μm, the depth set to 10 μm, and automated thresholding. As presented, images were stitched together from 20 smaller images to produce an image with FOV 300 × 300 μm using 25% overlap. Stitching, flattening, leveling, and masking operations were made to unify the stitched FOV in Vision 64 and MountainsMap (v7.4)

https://doi.org/10.1021/acsapm.2c01477
ACS Appl. Polym. Mater. 2023, 5, 1670−1680

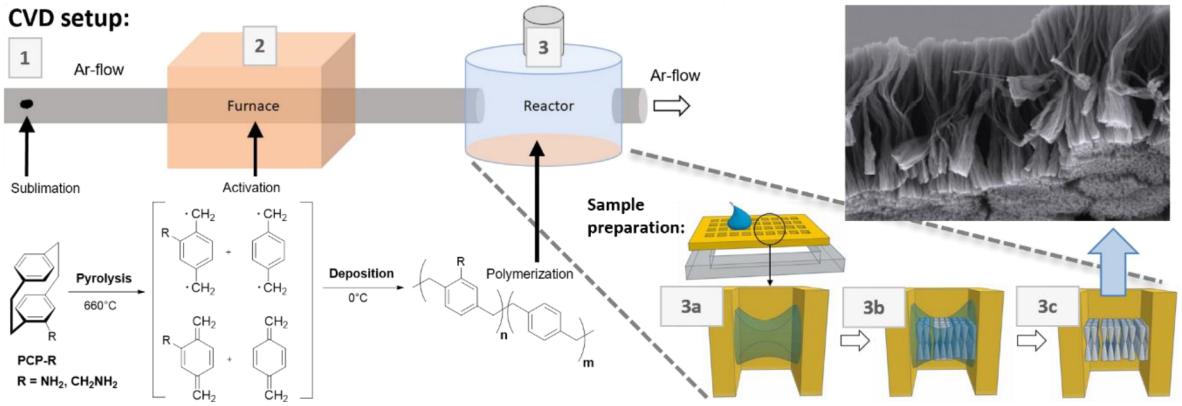

Figure 1. Fiber Growth. Solvent-less CVD polymerization to form free-standing nanofiber. (1) Initially, the precursor monomers (either PCP-CH_2NH_2 or PCP-NH_2) are sublimed with heat under vacuum. (2) Argon (carrier gas) transports the monomers into a furnace (660 °C) and converts them pyrolytically into reactive intermediates. (3a) The reactive intermediate is carried into the reactor chamber where the LC substrate resides. (3b) The intermediates dissolve into the aligned, nematic LC (E7) suspended film, and fibers are grown. (3c) Removal of the LC results in a porous aligned nanofiber array.

software. For minimizing the signal to noise-ratio, the device was positioned on a vibration-damping table in a class 10,000 cleanroom.

Fluorescence Microscopy. Microscopic measurements were obtained using a Nikon Eclipse 80i microscope, equipped with an X-Cite Series 120Q (ExFo) excitation source, Photometrics CoolSnap EZ CCD camera, and NIS Elements software (Nikon, v5.20.02); quantitation was performed using the FIJI distribution of ImageJ (v1.53c) with data presentation in Origin Pro (v9.9.0.225). A filter cube appropriate for DAPI excitation and emission was used (360/30 excitation filter, 465/30 emission filter, and 450 nm dichroic mirror). For all samples, a collection of the fluorescence images occurred with 20 ms integration time and a gain of 1 with a 10× lens; phosphorescence images were obtained through 2 min of exposure to excitation, delivered through a 4× lens followed immediately by blocking of the excitation source, and the initiation of imaging with a 10× lens (<1 s between steps); an integration time of 20 s was used for the collection of the phosphorescence images.

Scanning Electron Microscopy. An environmental scanning electron microscope, Thermo Fisher Scientific Quattro, was used to inspect nanoscale system features. Backscattered electron images were taken with a concentric backscattered detector at an accelerating voltage of 8 kV and a working distance of ca. 9 mm. Secondary electron images (Supporting Information) were recorded with an Everhart−Thornley detector at a working distance of 10 mm and an accelerating voltage of 3 kV. Prior to these investigations, the samples were coated with a conductive layer of approx. 2 nm Pt (Hochvakuum-CoaterLeica EM ACE600). Scanning electron micrographs presented in Figure S3 were sputtered with a 3 nm thick gold layer and analyzed with a Zeiss LEO 1530 SEM, with an InLense detector, EHT of 7 kV, and a working distance of 2.76 mm. By inspection, values higher than 8 kV EHT not recommended since they can induce a phase transition in the polymer (i.e., melting).

Atomic Force Microscopy. Atomic force microscopy (AFM) measurements were performed with a Veeco Dimension Icon Atomic Force Microscope (Bruker, USA) operated in PeakForce Quantitative Nanoscale Mechanical mode. A Scanasyst-Fluid probe (Bruker, USA) was used, with nominal values of k = 0.7 N/m, radius = 20 nm, and = 150 kHz. The probe oscillated along the vertical axis in off-resonance at 2 kHz. The image resolution was 256 × 256 pixels, and the analysis of the AFM data was performed by Nanoscope Analysis software (Bruker, USA).

Photophysical Methods and Analysis. Emission and excitation spectra, as well as emission lifetime spectra, for both the membranes and bulk materials were obtained with a QuantaMax (Horiba) spectrometer equipped with double monochromators, halogen and xenon lamps, a 360 nm picosecond diode laser (Delta Diode), a PMT detector, and time-correlated single-photon counting detector. Excitation and emission spectra were taken at 1 nm increments (2 nm slit width for both monochromators). TCSPC measurements were obtained using 360 nm excitation operated at a frequency of 10 MHz, with a collection wavelength of 425 nm (14 nm slit width). Phosphorescence measurements were obtained with xenon lamp illumination (360 nm excitation, 14 nm slit width, 1000 Hz) and collection at 425 (14 nm slit width). All nanofiber film measurements were obtained from duplicate samples that were then each measured in triplicate from different regions of the films with analysis performed on the average for each sample for each method. No significant differences between duplicates were observed. Bulk films were measured in triplicate. Analysis was performed in Origin (OriginLabs, v9.8) for steady-state measurements. Emission lifetime measurements were assessed using DecayFit (fluorotools.com, v1.4) through deconvolution of the instrument response function (IRF). Decay results were then confirmed through re-convolution in Origin. All graphical results were presented with Origin. Fluorescence and phosphorescence average lifetimes are calculated from $\tau_{avg} = \Sigma(a_i t_i^2)/\Sigma(a_i t_i)$ from the component lifetimes (presented in Supporting Information).

RESULTS AND DISCUSSION

Herein, we report a LC-templated CVD polymerization approach to build free-standing poly(*p*-xylylene)-based membranes with high lateral order that exhibit long-lived solid-state luminescent properties at room temperature. While it was previously observed that [2.2]paracyclophane derivatives possessed some long-lived emission (seconds-scale) when frozen in ethanol at 77 K by Hopf and co-workers,[34] these small molecules were also found to be effectively nonemissive at room temperature. Our hypothesis that aligned nanofiber structures can contribute to long-lived emission will be explored via wide-field emission microscopy, steady-state spectroscopy, and through emission lifetime studies.

Prior studies by our team[30,31,35] have included the preparation of unidirectional LC-templated surface-aligned nanofibers that were synthesized via CVD polymerization. Additionally, the feasibility of air-supported LC systems has been reported by Hartono et al.[36−38] Lastly, extensive characterization of this class of polymers has been done to confirm both polymer structure and the retention of substituted functional groups.[39−43] In this work, the two strategies (LC templating with free-standing LCs) were combined for the purpose of generating free-standing nanofiber polymer membranes (Figure 1). A detailed procedure for the formation of those membranes via LC-templated CVD

https://doi.org/10.1021/acsapm.2c01477
ACS Appl. Polym. Mater. 2023, 5, 1670−1680

polymerization in air-suspended LC films has been given in the experimental section (flow rate 20 SCCM, 21.6 mg monomer, 660 °C furnace, −10 °C deposition stage). Multiple additional batches were generated with varying monomer mass (5.4−21.6 mg) and deposition stage temperature (−15 to 0 °C) to explore the design space. Carbon-free TEM grids (copper, 200 × 200 μm pores) were utilized as an array of wells for the suspension of LC materials into a collection of free-standing films. Under these conditions, the LC films undergo homeotropic alignment, which is assisted by two air−LC interfaces at the top and bottom of the grid pore. This strategy is different from previous efforts to generate CVD polymerized nanofiber arrays, in that there is no solid-state substrate to direct the LC orientation. Subsequent CVD polymerization of PCP-NH_2 and PCP-CH_2NH_2 precursors into the homeotropic-aligned layer (nematic LC, E7) was performed leading to the formation of unidirectional assembled free-standing polymer membranes within the wells of the TEM grids. These free-standing membranes, which comprises laterally organized hourglass-shaped nanofiber architectures, possessed emergent photophysical properties notably different, potentially more useful than the properties of the bulk polymers.

After membrane/fiber growth, topologic and geometric features of the nanofiber membranes were analyzed by VSI (Figure 2), scanning electron microscopy (SEM) (Figure 3), and AFM (Figure 4). AFM measurements were done to observe the long-range (micro-) and short-range (nano-) features of membrane surfaces. SEM imaging analysis indicated the formation of hourglass-shaped fiber arrays assembled to laterally aligned membranes. Remarkably, the membrane's total surface area (internal and external) increased 71-fold compared to a non-nanostructured uniform film of the same material, as calculated by image analysis. Detailed information about the chemical composition of 4-(amino)- and 4-(aminomethyl)-substituted poly-*para*-xylylene structures via X-ray photoelectron spectroscopy (XPS), as well as the evidence of the homeotropic LC alignment by polarized optical microscopy, is presented in Figures S1 and S2. Wide scan XPS results provided atomic C:N ratios of 16:1.1 and 17:0.9 for the PPX-NH_2 and PPX-CH_2NH_2 systems (respectively), aligning well with the anticipated 16:1 and 17:1 ratios.

Interferometric measurements confirmed the retention of air-suspended LC films inside a single TEM-grid cell before CVD polymerization (Figure 2). These measurements were repeated after polymerization, both before and after the removal of the LC. Observation of the topography from measurements of the top of the films allowed for the assessment of surface curvature and/or homogeneity. Inspection of the templated nanofiber bilayer (after LC removal) indicated the formation of a homogenous micro-assembled polymer layer. Direct observation resulted in a notable change in the appearance of the LC films. In Figure 2, a compilation of 3D optical micrographs is presented. The respective surfaces for individual wells were scanned in three states: (1) LC-only, (2) polymer in LC, and (3) polymer without LC. Differences in surface roughness can be observed when comparing LC-only to the polymer films, which is to be expected. Within the LC-filled well, a convex shape could be observed indicating normal capillary-like behavior (Figure 2a), with a parabolic slope toward the edges.[38,44] Analysis of the polymer-in-LC membrane showed both rough and planar characteristics (Figure 2b), with some residual ascent toward the grid surface

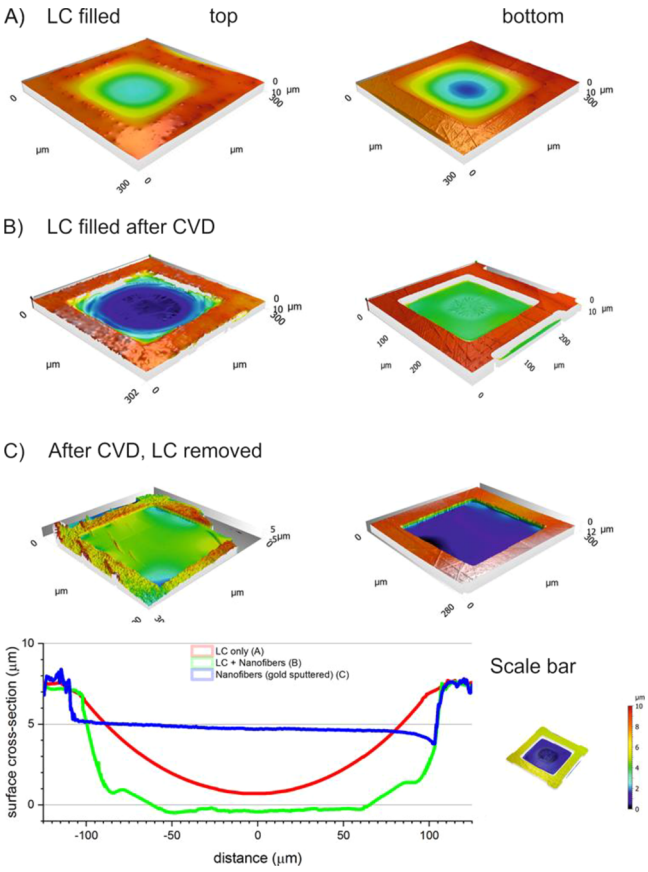

Figure 2. Interferometry of film surfaces. Cross-sections extracted from 3D depiction using vertical scanning interferometry (VSI) at the top and bottom sides over a total distance of 300 μm; (A) air-suspended LC film retained inside a 200 μm well, before the CVD polymerization; (B) formation of the free-standing nanofiber membranes without the LC being removed after CVD polymerization; (C) membranes after LC removal and sputtering. The 7.5 μm depth of the deepest feature aligns well with the midpoint of the grid thickness (15 μm, nominal).

at the edges (attributed to LC capillary action). The sputtered surface of the polymer-only membrane (Figure 2c) indicated uniformity and low roughness. Overall, VSI measurements support the initial hypothesis of air-suspended LC films being retained inside the TEM-grid wells. Additionally, the LC-removed polymer membranes presented a uniform surface that possessed no apparent warping at the edges. This is consistent with a minimum energy gradient that favors the center of the LC substrate. Though these measurements are appropriate for the inspection of the differences in shape and roughness over 10 and 100 s of microns, it is critical to assess the nanodomain features of these materials. Therefore, SEM analysis was conducted as follows, to obtain insight into the micro- to the nanostructure of the membrane.

Given the structure of the free-standing nanofiber arrays, a detailed characterization was performed to help understand the origin of the luminescent properties. SEM micrographs of the free-standing polymer film reveal both micro- and nanoscale structure (Figure 3), presenting as hourglass-shaped fibrils that laterally align as biconical bundles, which in turn assemble into continuous nanofiber arrays with higher porosity in the center than toward the surface. In addition to observing the general film features, care was taken to evaluate the biconical fibers

https://doi.org/10.1021/acsapm.2c01477
ACS Appl. Polym. Mater. 2023, 5, 1670−1680

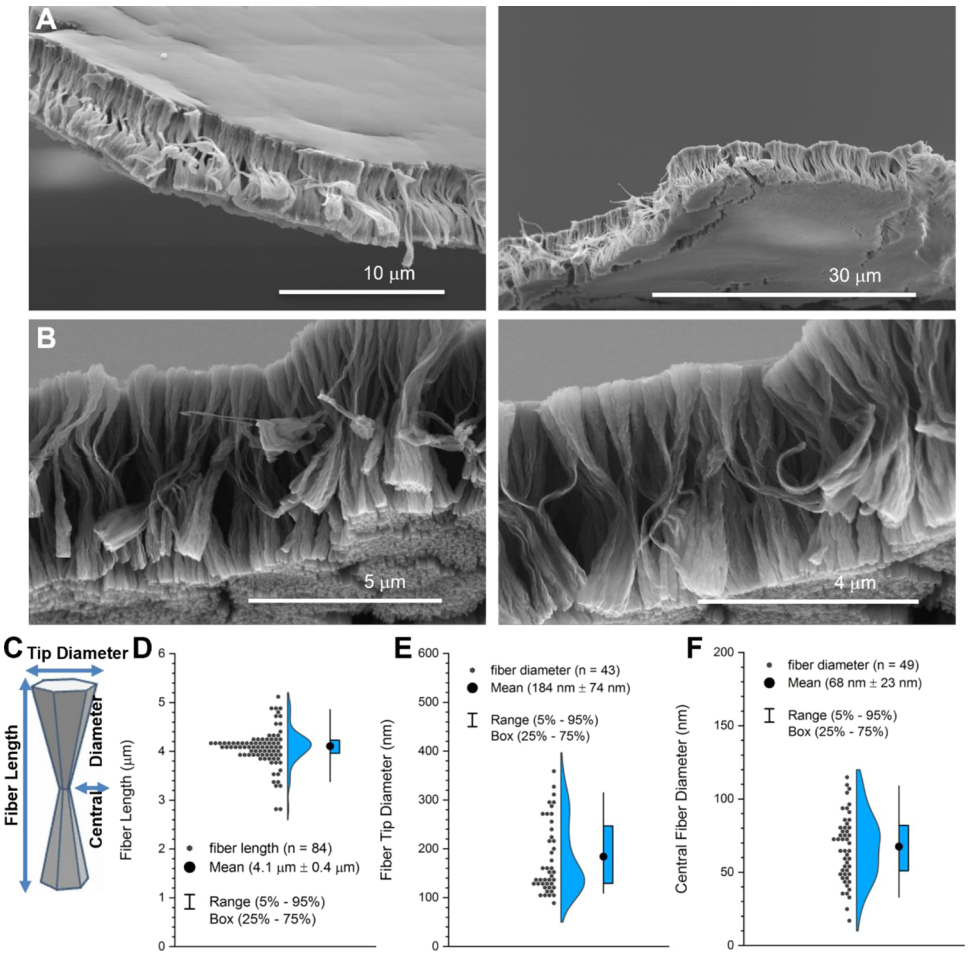

Figure 3. Dimensional analysis of free-standing nanofiber membranes. (A,B) SEM images of the lateral organized free-standing nanofiber membranes; (C) 3D rendering of the model used for surface area and porosity calculations; (D) distribution of fiber lengths; (E) distribution of fiber tip diameters; and (F) distribution of central fiber diameters. The left image in (A) shows the top view of the free-standing film, where the upper surface resembles a uniform coated film. In contrast, the right image in (A) represents the bottom view, where the film resembles a regular semiporous surface. Observations in (A) indicate a sterically favored access of the reactive intermediate from the top, resulting in a lower amount of polymer on the bottom side of the "semisealed" porous network. This effect was consistent across all samples. (B) shows the cross-section of the film, displaying the hourglass shape of individual fibers with an outer diameter that differs from the center diameter. The cross-sections also show the regular alignment of the free-standing fibers to a porous network.

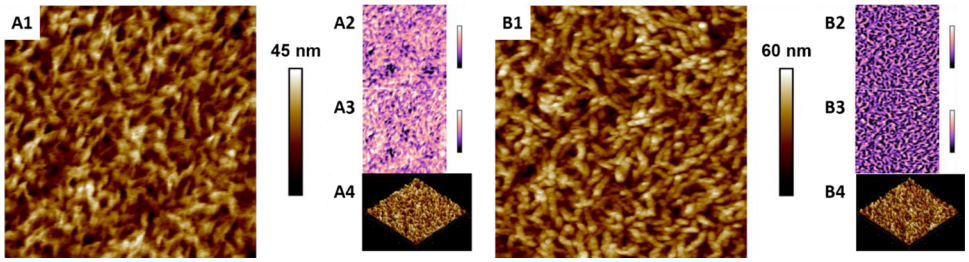

Figure 4. AFM Analysis of PPX-CH_2NH_2 Fibers with and without LC. With LC: (A1) AFM Topographic; (A2) adhesion; (A3) dissipation; (A4) 3D topography; without LC: (B1) AFM topographic; (B2) adhesion; (B3) dissipation; (B4) 3D topography. Field of view: 5 × 5 μm. Adhesion and dissipation scales are in arbitrary units (a.u.).

that appear to be building blocks for the membrane. In total, images from seven batches produced under identical conditions were analyzed via ImageJ (8-bit images, pixel aspect ratio = 1). A total of 176 measurements were taken to include measurement of the following: end and middle diameter of the biconical fiber structure and the total fiber length (Figure 3c), approximated later as hexagonal overlapping cones.

Both the top and bottom surfaces were observed along an incision. The top of the film appeared to have merged into a continuous film with no visible gaps between the fibers (Figure 3a, left). The bottom surface of the film was slightly less uniform, with evidence that unity was not obtained (Figure 3a, right). Contrast thresholding of the images revealed approximately 11% (+/−1%) of the bottom surface manifested as gaps between fibers and fiber bundles. This is attributed to

https://doi.org/10.1021/acsapm.2c01477
ACS Appl. Polym. Mater. 2023, 5, 1670−1680

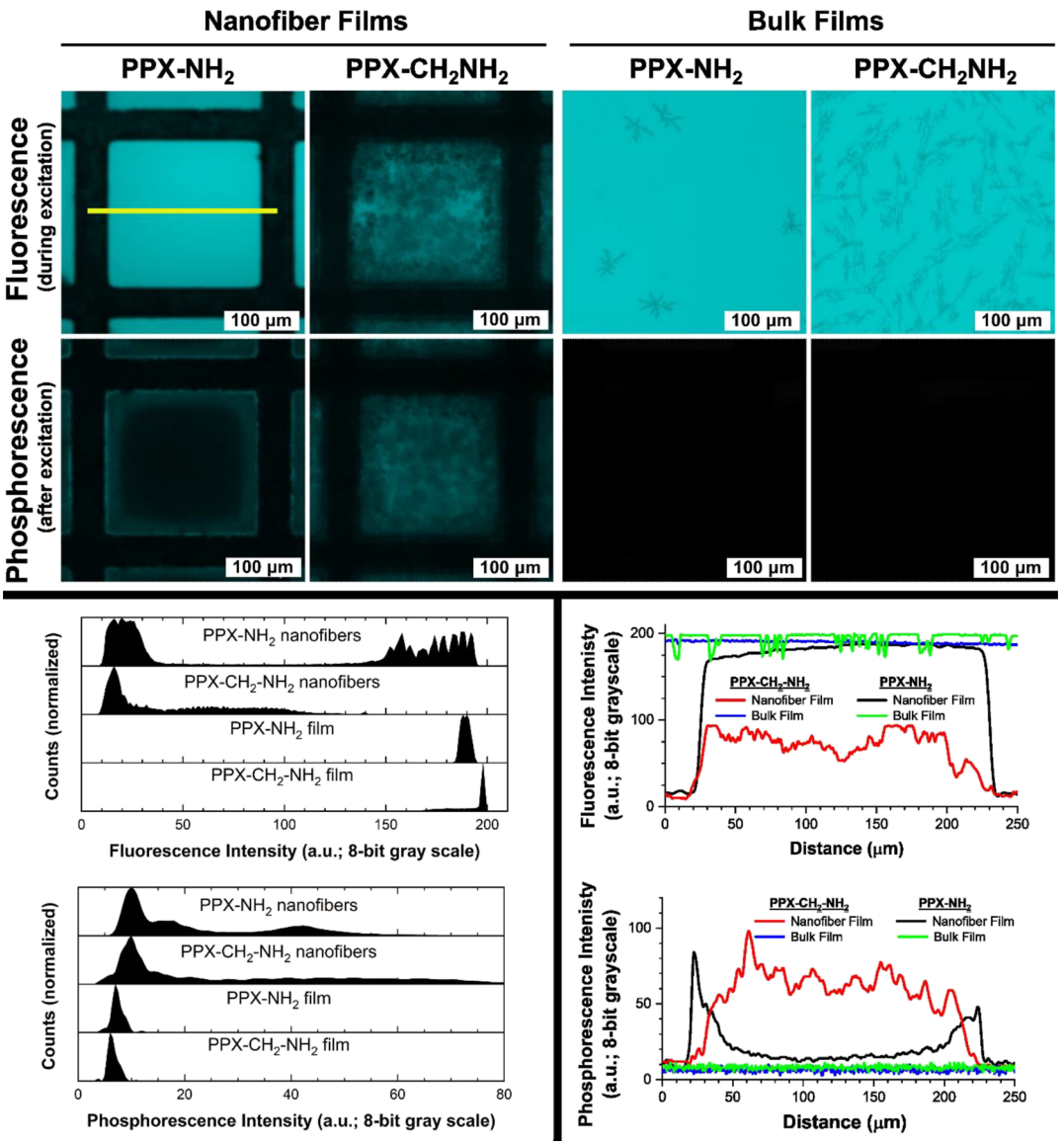

Figure 5. Microscopic wide-field emission studies. Fluorescence and phosphorescence images of the nanofiber and bulk films (top). Full field-of-view intensity histograms for each image (bottom left). Line intensity plots for identical regions of interest; ROI identical to the line in the first image presented (bottom right).

direction of monomer arrival, whereby the likelihood of monomer penetration from the bottom was lower than from the top, which is reasonable from a diffusion standpoint; this in turn led to a decrease in growth at the bottom surface.

The total surface area of the entire film was calculated from measured feature sizes of the fibers: end diameter (184 nm ± 74 nm, n = 43), central minimum diameter (68 nm ± 23 nm, n = 49), and total fiber length (4.1 μm ± 0.4 μm, n = 84) (Figure 3d–f). The average aspect ratio was then calculated to be 22.3. From this, the total surface area of the membrane (external and internal area) was calculated from the superposition of two conjoined frustums of regular hexagonal pyramids (Figure 3c). A hexagonal architecture was chosen over a conical structure for the calculation due to the nature of the fibers and fibrillar substituents (i.e., hexagonal approximation of close packing of strands/fibrils and hexagonal approximation of close packing of hexagons to obtain unity on a 2D plane). A correction to the size of the frustum (bottom half of the fiber) was made based on the measurement of the gaps in the bottom face, reducing the area of the largest hexagonal face by a proportionate amount. These calculations provide a total surface area of 1.6 μm^2 per fiber or 71 cm^2 per 1 cm^2 of film (as viewed from above). The porosity ($1 - V_{fiber}/V_{unit\ cell}$) was calculated to be 52%, with the average fiber volume being 0.043 μm^3. In terms of pore volume per unit area of film, 1 cm^2 of the film generates 214 nL of pore volume, as shown in Figure 3. In general, across all films, we observed a film-like structure across the top and bottom surfaces of the membrane. However, defects were also routinely observed. For completeness, some defects (e.g., insufficient LC-filling, rupture occurring during CVD polymerization/sputtering, workup, and handling) are presented in Figure S3a–d.

In addition, AFM was performed to assess the top surfaces of the films; this was done for the PPX-CH_2NH_2 system with and without liquid crystal template material present (Figure 4). Height profile micrographs are presented in Figure 4, including relative adhesion, relative dissipation, and a 3D rending of the topography (obtained fast-force mapping off-resonance tap-

https://doi.org/10.1021/acsapm.2c01477
ACS Appl. Polym. Mater. 2023, 5, 1670−1680

Table 1. Quantitative Analysis of the Steady-State and Fluorescence and Phosphorescence Lifetime Study[a]

		steady state					time-resolved emission			
material	sample	$excitation_{max}$ nm	$emission_{max}$ nm	$bandgap_{S0\rightarrow S1}$ eV	$bandgap_{S1'\rightarrow S0'}$[b] eV	Stokes shift eV	$I_{FL,sum}$	$\tau_{FL,avg}$ ns	$I_{PH,sum}$	$\tau_{PH,avg}$[c] μs
$PPX\text{-}CH_2NH_2$	nanofiber film	380	428	3.26	2.90	0.37	0.89	2.5 ± 0.5	0.11	4.5 ± 1.0
	bulk film	376	428	3.30	2.90	0.40	1.00	3.8 ± 0.1		
$PPX\text{-}NH_2$	nanofiber film	380	422	3.26	2.94	0.32	0.91	2.6 ± 0.5	0.09	4.3 ± 1.0
	bulk film	376	422	3.30	2.94	0.36	1.00	3.7 ± 1.0		

[a]Excitation observed for 425 nm emission; emission observed from 370 nm excitation. Time-resolved measurements with 360 nm excitation and 425 nm emission. [b]Includes $T_1 \rightarrow S_0$ for both nanofiber samples. [c]Both nanofiber samples possessed observable, long (>1 ms) emission consisting of <0.1% of the total emission.

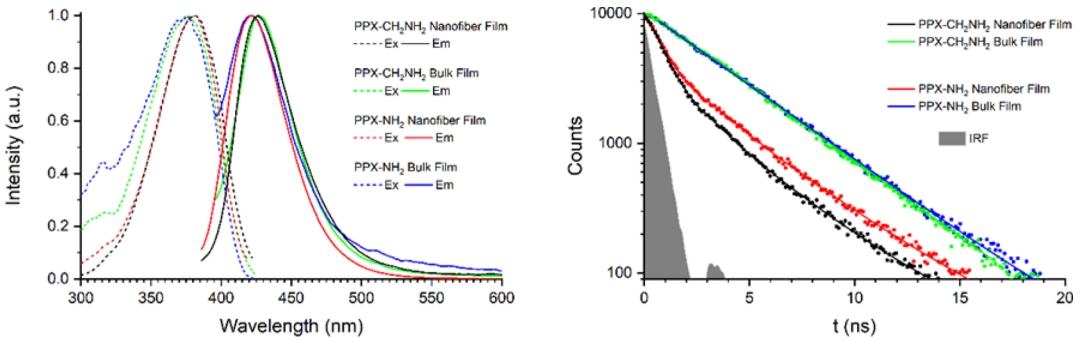

Figure 6. Steady-state (left) and lifetime studies (right). The decay profiles for the lifetime studies were monitored at 425 nm emission for the nanofiber membranes and bulk films of $PPX\text{-}CH_2NH_2$ (black, green) and $PPX\text{-}NH_2$ (red, blue), respectively. The excitation wavelength is 360 nm. The fiber membranes display the emergence of a multicomponent decay, a tell-tail sign of competing pathways (such as intersystem crossing).

ping mode). 3D renderings with overlays are provided in Figure S6. Qualitative inspection of the two surfaces displayed subtly differing structures with and without the LC. The fibers with LC presented as tapered, spine-like sharp structures with an overall feature height that is lower than the fibers without LC. The features without LC appeared to be cylindrical with tips laying oriented to the substrate. The average diameters observed were 63 nm ±14 nm and had lengths of 213 nm +/− 42 nm; these dimensions are consistent with fibrils forming features on a surface that is largely uniform on the microscale. The tapered structures observed in the sample with LC present longest-axis lengths of 151 +/−26 nm. In the absence of the LC matrix, the structures appeared to represent fibral ends. The overall depth of view difference indicates that removal of the LC did not cause the fibers to collapse (i.e., decrease in depth of view), and LC removal allowed the AFM probe image further into the fiber array. Mapping of the surface for variation in relative adhesion force (arbitrary units) and relative dispersion energy (arbitrary units) provides additional information regarding the features observed. Specifically, both samples present higher dispersion and adhesion between features with a subtle difference between the two; the LC-free fibrils display low values for dispersion and adhesion over their entire structures, while the LC fibrils only present low values at the tip of the topographic features. This indicates an AFM tip interaction with the top layer of the LC-fiber structure only; this further supports a capillary-type LC interaction with the fibers, as well as a fibral occupying the center of each feature. In total, these results are consistent with the SEM results and provide insight into the nature of the post-polymerization interactions between the LC and the resultant fibers/fibrils.

Fluorescence microscopy reveals autofluorescence of the free-standing nanofiber system (Figure 5). Initially, qualitative investigations were undertaken by utilizing an upright fluorescence microscope. Using 360 nm (360/30) excitation and 465 nm (465/30) collection filters, images were obtained under identical working conditions for the nanofiber and bulk films as reference materials (see methods). Both fluorescence (during excitation) and phosphorescence (after excitation) images were obtained (Figure 5). Inspection of emission histograms for the entire FOV provided the following insights: (1) the fluorescence images of the bulk films were brighter than either of the nanofiber films; (2) the fluorescence from $PPX\text{-}NH_2$ nanofiber films was brighter and more uniformly bright than the $PPX\text{-}CH_2NH_2$ nanofibers, which exhibited a more irregular emission pattern on the microscale; (3) the phosphorescence images from both bulk films indicated no phosphorescence; and (4) phosphorescence (20 s collection after excitation) of the $PPX\text{-}CH_2NH_2$ nanofiber film was brighter and spanned the entire film, while the $PPX\text{-}NH_2$ nanofiber film was brightest near the edges of the cavity and overall less bright (especially in the center of the cavity). These results provide evidence of the initial observation of phosphorescence from the nanofiber films and align well with fluorescence lifetime and phosphorescence lifetime studies, presented later. Specifically, fluorescence brightness follows the fluorescence lifetime trends (bulk films > $PPX\text{-}NH_2$ nanofibers > $PPX\text{-}CH_2NH_2$ nanofibers) and phosphorescence brightness follows the phosphorescence trends ($PPX\text{-}CH_2NH_2$ nanofibers > $PPX\text{-}NH_2$ nanofibers ≫ bulk films). This provides evidence of the of structure-induced intersystem crossing initially posited, justifying subsequent steady-state and lifetime studies (Table 1).

Photophysical Analysis as a Quantification of the Appearing Fluorescence and Phosphorescence of the Tapered Free-Standing Nanofiber Bilayer System. In addition to the discovery of luminescence during microscopic inspection of the films, photophysical analysis was conducted

https://doi.org/10.1021/acsapm.2c01477
ACS Appl. Polym. Mater. 2023, 5, 1670−1680

to understand the impact of the nanostructure on the emission properties (Figure 6). All samples, nanofibers, and bulk films had similar excitation and emission profiles with a few subtle differences. Both nanofiber films had similar excitation maxima (380 nm) with the bulk films both slightly blue-shifted (376 nm) from the nanofibers. Despite excitation similarities between the nanofiber films and between the bulk films, the emission profile similarities corresponded with the chemical composition. Both, the nanofiber and bulk films comprised of PPX-CH_2NH_2, expressed identical emission maxima (428 nm). The PPX-NH_2 films also express identical emission maxima (422 nm) blue-shifted relative to the PPX-CH_2NH_2 systems. The Stokes shift of both nanofiber systems was found to be smaller than that of the bulk films made from identical precursors. These results imply that the polymer systems themselves inherently possess excitation and emission properties that are sensitive to neighboring polymer regions.[1,9,18,45,46] The decreased Stokes shift of the nanofiber systems indicates a slight constraining effect that either disrupts these interactions (smaller shift) or provides an alternate pathway for relaxation (apparent decrease in shift due to loss of lower-lying states to alternate processes).

Time-correlated single photon counting was performed on all samples (nanofibers and bulk films, 360 nm excitation, 425 nm emission) to assess the impact of nanostructure on emission properties. Both bulk films expressed comparable single exponential decay (3.7−3.8 ns) with no evidence of ultrafast emission (<1 ns) or long-lived residual emission (>100 ns). Both nanofiber membranes expressed significantly shorter average lifetimes (τ_{avg} 2.4−2.5 ns) than those observed in the bulk films; they also clearly possessed multiexponential decay with component fractions that differed from each other (Supporting Information, "Photophysical Methods and Analysis for the Determination of Phosphorescence Lifetime"). While the nanofiber emission lacked evidence of ultrafast relaxation processes, similar to the bulk films, the nanofiber membranes possessed long-lived residual emission tails (<0.1% of the peak intensities) that indicated a longer-lived emissive state. A long-lived tail was not observed for either bulk film. Direct inspection of the decay traces (Figure 6, right) suggests that both nanofiber membranes experience competing relaxation pathways that are not present in the bulk film, with the PPX-CH_2NH_2 nanofiber film displaying this effect to a greater degree than the PPX-NH_2 nanofiber film. In total, these results indicate that the bulk films lack a phosphorescent relaxation pathway. In contrast, this relaxation pathway must exist for the nanofiber arrays, as indicated by the nanostructural effect on emissivity and the excited state relaxation pathways allowed for each system.

Emission lifetimes in the μs regime further confirmed the existence of measurable luminescence from the nanofiber films at longer timescales (360 nm excitation, 425 nm emission). In contrast, measurements of the bulk films returned only the IRF of the xenon lamp source, indicating that no long-lived emission was occurring in these systems. Both of the nanofiber films provided a measurable phosphorescent signal that differed from the IRF. These could be deconvolved from the IRF, returning phosphorescent lifetimes that were comparable for both systems (4.3−4.5 μs). Additionally, normalization of the IRF and the emission traces allowed for the determination of the contributions to emission occurring from within the IRF (fast, ns regime) and the emission associated with the phosphorescence. Notably, both nanofiber films possessed a discernable very long-lived (>1000 μs, <0.1%) emission that confirmed the direct observation of emission continuing for seconds after excitation, which were the basis for photophysical investigations. These observations are in accordance with systems found in literature describing solid-state phosphorescent properties at room temperature derived from distinct packing modes; examples include single-crystalline or polymer structures with a suitable chemical composition for $\pi-\pi$, intermolecular, and dipole−dipole interactions, as well as $n-\pi^*$ transitions.[1,2,47]

Collectively, the steady-state and emission decay studies suggest that both the molecular makeup and the nanofiber structural constraint of the systems play a role in emission properties. The most important findings are that interconversion to a long-lived emission state is only possible for the nanofibers and that this state is more accessible to the PPX-CH_2NH_2 nanofibers than to the PPX-NH_2 (as confirmed through fluorescence lifetime traces and the amount of long-lived emission relative to total emission).[48,49] Some reports indicate that the surfaces of organic nanostructures are capable of exhibiting emissive properties that are markedly different than that of bulk or internalized materials.[9,46] Given the high surface-to-volume ratio of these nanofiber films, this may also serve to explain the emergence of the phosphorescence observed in these systems, especially if the LC template during growth provides local environments not found in the bulk. These findings open the path for potential PPX usage in the areas of optoelectronics or bioimaging.[50] While the re-emergence of emission with polymerization is interesting, the evolution of a long-lived emission from nanostructuring of the polymer is doubly so. It was also observed that short-lived (ns regime) emission could be observed in the bulk polymer, though no evidence a long-lived emission was found in the unstructured film. The structure-induced long-lived emission, in combination with increased surface area, indicates a potential use in polymer-based soft matter sensors or through expansion into chiral and/or electro-actuating systems.[51,52]

CONCLUSIONS

This work presents poly(*p*-xylylene)-based, laterally organized nanofiber membranes that exhibit long-lived emission at room temperature. Important properties of these free-standing nanofiber membranes include high surface area and porosity, nanoscale and microscale order, intrinsic luminescence, and long-lived emission that is not observed in bulk polymers.

Regarding the morphological studies, depth profiles of VSI optical micrographs scanned from the top and bottom surface corroborated the assumption of the air-suspended LC film being retained before CVD polymerization. Moreover, inspection and image analysis of SEM micrographs revealed the formation of hourglass-shaped single fibers, laterally aligning to a free-standing network. The fiber tip diameters were found to be ca. 200 nm, with fiber lengths closer to 4 μm, and an average aspect ratio of ca. 22. To that effect, both total fiber surface area (71 $cm^2/1$ cm^2 of the film) and porosity (52%, 214 nL/cm^2 of film) were calculated from the results of the SEM study. The surface of the LC-filled and LC-removed films was investigated with AFM, supporting the SEM results. The tips of fibrils were observed with an overall indication that removal of the LC did not cause the fibers to collapse.

Optical microscopy inspection of the nanofiber membranes exhibited both short-lived (direct excitation, fluorescence) and long-lived, luminescence after excitation. Further, comparative

https://doi.org/10.1021/acsapm.2c01477
ACS Appl. Polym. Mater. 2023, 5, 1670−1680

microscopy studies of both free-standing nanofiber systems with conformal films of analog chemical components were undertaken; this showed inverse trends for fluorescence and phosphorescence intensities for the nanofiber membranes versus homogeneous films and no observation of phosphorescence in the conformal films. In addition, photophysical steady-state studies revealed similar excitation and emission maxima for the nanofiber membranes and homogeneous films, with the films' excitation maxima slightly blue-shifted (376 nm) from that of the membranes (380 nm). The emission maxima (428 nm) were found to be identical to nanofiber membranes and homogeneous films. Fluorescence and phosphorescence lifetime studies were significant in revealing the impact of the nanofiber confinement on the emission properties. While the nanofiber membranes possessed a multiexponential decay in ps-ns TCSPC studies, only a single exponential decay was observed for the films. This further strengthened the claim that structural confinement is responsible for phosphorescent relaxation and emissivity. Direct observation, microscopic studies, and the TCSPC result all indicated a singlet to triplet interconversion and structure-induced intersystem crossing, warranting formal phosphorescence lifetime studies. Both of the nanofiber films provided a measurable phosphorescent signal in the 4.3−4.5 μs regime and emission lifetimes. For both film systems, a long-lived (>1000 μs, <0.1%) emission could be found, likely the source of the initial microscopic observation. The occurrence of phosphorescence for both the PPX-NH_2 and the PPX-CH_2NH_2 nanofiber systems indicates a high potential for use as biomimetic material and soft matter sensors.

Lastly, this work extends the dimensionality of prior substrate-bound LC-templated nanofibers into porous, high-surface-area, emissive membranes of hourglass-shaped nanofiber. Taken together, morphologically controlled polymer membranes with long-lived emission establish a substrate-independent platform that offers a variety of opportunities for future applications where emissive (possibly self-reporting) nanosensors or nanomembranes are required.

■ ASSOCIATED CONTENT

Supporting Information

The Supporting Information is available free of charge at https://pubs.acs.org/doi/10.1021/acsapm.2c01477.

Polarized optical microscopy, XPS spectra, scanning electron microscopy, growth mechanism discussion, atomic force microscopy, flash photolysis spectra, and Raman spectra (PDF)

■ AUTHOR INFORMATION

Corresponding Author

Joerg Lahann − *Soft Matter Synthesis Laboratory, Institute for Biological Interfaces 3 (IBG-3) and Institute of Functional Interfaces (IFG), Karlsruhe Institute of Technology (KIT), Campus North, 76344 Eggenstein-Leopoldshafen, Germany; Biointerfaces Institute (BI), University of Michigan, Ann Arbor, Michigan 48109, United States;* orcid.org/0000-0002-3334-2053; Email: lahann@umich.edu

Authors

Mirella Wawryszyn − *Soft Matter Synthesis Laboratory, Institute for Biological Interfaces 3 (IBG-3), Karlsruhe Institute of Technology (KIT), Campus North, 76344 Eggenstein-Leopoldshafen, Germany*

Robin Wilhelm − *Institute of Functional Interfaces (IFG), Karlsruhe Institute of Technology (KIT), Campus North, 76344 Eggenstein-Leopoldshafen, Germany*

John Kim − *Biointerfaces Institute (BI), University of Michigan, Ann Arbor, Michigan 48109, United States*

Xiaoyang Zhong − *Biointerfaces Institute (BI), University of Michigan, Ann Arbor, Michigan 48109, United States*

Jeffery E. Raymond − *Biointerfaces Institute (BI), University of Michigan, Ann Arbor, Michigan 48109, United States;* orcid.org/0000-0002-4414-1898

Richard Thelen − *Institute for Microstructure Technology (IMT) and Karlsruhe Nano Micro Facility (KNMFi), Karlsruhe Institute of Technology (KIT), Campus North, 76344 Eggenstein-Leopoldshafen, Germany*

Vanessa Trouillet − *Institute for Applied Materials (IAM-ESS) and Karlsruhe Nano Micro Facility (KNMFi), Karlsruhe Institute of Technology (KIT), Campus North, 76344 Eggenstein-Leopoldshafen, Germany*

Matthias Schwotzer − *Institute of Functional Interfaces (IFG), Karlsruhe Institute of Technology (KIT), Campus North, 76344 Eggenstein-Leopoldshafen, Germany*

Stefan Bräse − *Institute of Biological and Chemical Systems (IBCS-FMS), Karlsruhe Institute of Technology (KIT), Campus South, 76131 Karlsruhe, Germany;* orcid.org/0000-0003-4845-3191

Do Hoon Kim − *Biointerfaces Institute (BI), University of Michigan, Ann Arbor, Michigan 48109, United States*

Nicholas L. Abbott − *Robert Frederick Smith School of Chemical and Biomolecular Engineering, Cornell University, Ithaca, New York 14853, United States;* orcid.org/0000-0002-9653-0326

Complete contact information is available at: https://pubs.acs.org/10.1021/acsapm.2c01477

Notes

The authors declare no competing financial interest.

■ ACKNOWLEDGMENTS

This work has been in part supported by the National Science Foundation through Grant 1916654 (J.L., N.L.A.). The authors also acknowledge technical support from the Michigan Center for Materials Characterization (https://mc2.engin.umich.edu/, University of Michigan). The cluster "3D Matter Made to Order" under Germany's Excellence Strategy (3DMM2O-EXC-2082-390761711, Thrust A1 and A2) is acknowledged for financial contributions (S.B.).

■ REFERENCES

(1) Yang, J.; Zhen, X.; Wang, B.; Gao, X.; Ren, Z.; Wang, J.; Xie, Y.; Li, J.; Peng, Q.; Pu, K.; Li, Z. The Influence of the Molecular Packing on the Room Temperature Phosphorescence of Purely Organic Luminogens. *Nat. Commun.* **2018**, *9*, 840.

(2) Hirata, S.; Totani, K.; Zhang, J.; Yamashita, T.; Kaji, H.; Marder, S. R.; Watanabe, T.; Adachi, C. Recent Advances in Materials with Room-Temperature Phosphorescence: Photophysics for Triplet Exciton Stabilization. *Adv. Opt. Mater.* **2017**, *5*, No. 1700116.

(3) Eder, T.; Stangl, T.; Gmelch, M.; Remmerssen, K.; Laux, D.; Höger, S.; Lupton, J. M.; Vogelsang, J. Switching between H- and J-Type Electronic Coupling in Single Conjugated Polymer Aggregates. *Nat. Commun.* **2017**, *8*, 1641.

(4) Mukherjee, S.; Thilagar, P. Recent Advances in Purely Organic Phosphorescent Materials. *Chem. Commun.* **2015**, *51*, 10988−11003.
(5) An, Z.; Zheng, C.; Tao, Y.; Chen, R.; Shi, H.; Chen, T.; Wang, Z.; Li, H.; Deng, R.; Liu, X.; Huang, W. Stabilizing Triplet Excited States for Ultralong Organic Phosphorescence. *Nat. Mater.* **2015**, *14*, 685−690.
(6) Zhang, Z.; Yan, W.; Dang, D.; Zhang, H.; Sun, J. Z.; Tang, B. Z. The Role of Amide (n,Π∗) Transitions in Polypeptide Cluster-oluminescence. *Cell Rep. Phys. Sci.* **2022**, *3*, No. 100716.
(7) Zhao, W.; He, Z.; Lam, J. W. Y.; Peng, Q.; Ma, H.; Shuai, Z.; Bai, G.; Hao, J.; Tang, B. Z. Rational Molecular Design for Achieving Persistent and Efficient Pure Organic Room-Temperature Phosphor-escence. *Chem* **2016**, *1*, 592−602.
(8) Gan, N.; Shi, H.; An, Z.; Huang, W. Recent Advances in Polymer-Based Metal-Free Room-Temperature Phosphorescent Materials. *Adv. Funct. Mater.* **2018**, *28*, No. 1802657.
(9) Raymond, J. E.; Ramakrishna, G.; Twieg, R. J.; Goodson, T. Two-Photon Enhancement in Organic Nanorods. *J. Phys. Chem. C* **2008**, *112*, 7913−7921.
(10) Baryshnikov, G.; Minaev, B.; Ågren, H. Theory and Calculation of the Phosphorescence Phenomenon. *Chem. Rev.* **2017**, *117*, 6500−6537.
(11) Wang, J.; Lou, X. Y.; Wang, Y.; Tang, J.; Yang, Y. W. Recent Advances of Polymer-Based Pure Organic Room Temperature Phosphorescent Materials. *Macromol. Rapid Commun.* **2021**, *42*, No. 2100021.
(12) Hong, Y.; Lam, J. W. Y.; Tang, B. Z. Aggregation-Induced Emission: Phenomenon, Mechanism and Applications. *Chem. Commun.* **2009**, *29*, 4332−4353.
(13) Gong, S.; Yang, C.; Qin, J. Efficient Phosphorescent Polymer Light-Emitting Diodes by Suppressing Triplet Energy Back Transfer. *Chem. Soc. Rev.* **2012**, *41*, 4797−4807.
(14) Sobhan, M. A.; Lebedev, A.; Chng, L. L.; Anariba, F. Rapid Fabrication of Photoluminescent Electrospun Nanofibers without the Need of Chemical Polymeric Backbone Modifications. *J. Nanomater.* **2018**, *2018*, 1.
(15) Itoh, T. Fluorescence and Phosphorescence from Higher Excited States of Organic Molecules. *Chem. Rev.* **2012**, *112*, 4541−4568.
(16) Kuzmitsky, V. A.; Gladkov, L. L.; Volkovich, D. I.; Solovyov, K. N. Density Functional Theory Calculations of the Lowest Excited Triplet State of the Closest Analogs of Chlorophyll and Bacterio-chlorophyll. *J. Appl. Spectrosc.* **2021**, *88*, 469−473.
(17) Kotkowiak, M.; Dudkowiak, A.; Fiedor, L. Intrinsic Photo-protective Mechanisms in Chlorophylls. *Angew. Chem., Int. Ed.* **2017**, *56*, 10457−10461.
(18) Raymond, J. E.; Bhaskar, A.; Goodson, T.; Makiuchi, N.; Ogawa, K.; Kobuke, Y. Synthesis and Two-Photon Absorption Enhancement of Porphyrin Macrocycles. *J. Am. Chem. Soc.* **2008**, *130*, 17212−17213.
(19) Varnavski, O.; Raymond, J. E.; Yoon, Z. S.; Yotsutuji, T.; Ogawa, K.; Kobuke, Y.; Goodson, T. Compact Self-Assembled Porphyrin Macrocycle: Synthesis, Cooperative Enhancement, and Ultrafast Response. *J. Phys. Chem. C* **2014**, *118*, 28474−28481.
(20) Park, Y.; Pravitasari, A.; Raymond, J. E.; Batteas, J. D.; Son, D. H. Suppression of Quenching in Plasmon-Enhanced Luminescence via Rapid Intraparticle Energy Transfer in Doped Quantum Dots. *ACS Nano* **2013**, *7*, 10544−10551.
(21) Wu, P.; Yan, X. P. Doped Quantum Dots for Chemo/Biosensing and Bioimaging. *Chem. Soc. Rev.* **2013**, *42*, 5489−5521.
(22) Teranishi, K. Localization of the Bioluminescence System in the Pileus of Mycena Chlorophos. *Luminescence* **2016**, *31*, 594−599.
(23) Chou, H. H.; Nguyen, A.; Chortos, A.; To, J. W. F.; Lu, C.; Mei, J.; Kurosawa, T.; Bae, W. G.; Tok, J. B. H.; Bao, Z. A Chameleon-Inspired Stretchable Electronic Skin with Interactive Colour Changing Controlled by Tactile Sensing. *Nat. Commun.* **2015**, *6*, 8011.
(24) Zhou, H.; Chua, M. H.; Tang, B. Z.; Xu, J. Aggregation-Induced Emission (AIE)-Active Polymers for Explosive Detection. *Polym. Chem.* **2019**, *10*, 3822−3840.
(25) Kwon, M. S.; Jordahl, J. H.; Phillips, A. W.; Chung, K.; Lee, S.; Gierschner, J.; Lahann, J.; Kim, J. Multi-Luminescent Switching of Metal-Free Organic Phosphors for Luminometric Detection of Organic Solvents. *Chem. Sci.* **2016**, *7*, 2359−2363.
(26) Wang, L.; Urbas, A. M.; Li, Q. Nature-Inspired Emerging Chiral Liquid Crystal Nanostructures: From Molecular Self-Assembly to DNA Mesophase and Nanocolloids. *Adv. Mater.* **2020**, *32*, No. 1801335.
(27) Cui, Y.; Liu, Y.; Liu, J.; Du, J.; Yu, Y.; Wang, S.; Liang, Z.; Yu, J. Multifunctional Porous Tröger's Base Polymers with Tetraphenylethene Units: CO2 Adsorption, Luminescence and Sensing Properties. *Polym. Chem.* **2017**, *8*, 4842−4848.
(28) White, T. J.; Broer, D. J. Programmable and Adaptive Mechanics with Liquid Crystal Polymer Networks and Elastomers Preparation and Properties of LCEs and LCNs. *Nat. Mater.* **2015**, *14*, 1087−1098.
(29) Cheng, K. C. K.; Bedolla-Pantoja, M. A.; Kim, Y. K.; Gregory, J. V.; Xie, F.; de France, A.; Hussal, C.; Sun, K.; Abbott, N. L.; Lahann, J. Templated Nanofiber Synthesis via Chemical Vapor Polymerization into Liquid Crystalline Films. *Science* **2018**, *362*, 804−808.
(30) Varadharajan, D.; Nayani, K.; Zippel, C.; Spuling, E.; Cheng, K. C.; Sarangarajan, S.; Roh, S.; Kim, J.; Trouillet, V.; Bräse, S.; Abbott, N. L.; Lahann, J. Surfaces Decorated with Enantiomorphically Pure Polymer Nanohelices via Hierarchical Chirality Transfer across Multiple Length Scales. *Adv. Mater.* **2022**, *34*, No. 2108386.
(31) Chen, H. Y.; Lahann, J. Designable Biointerfaces Using Vapor-Based Reactive Polymers. *Langmuir* **2011**, *27*, 34−48.
(32) Koenig, M.; Kumar, R.; Hussal, C.; Trouillet, V.; Barner, L.; Lahann, J. PH-Responsive Aminomethyl Functionalized Poly(*p* -Xylylene) Coatings by Chemical Vapor Deposition Polymerization. *Macromol. Chem. Phys.* **2017**, *218*, No. 1600521.
(33) Lahann, J.; Klee, D.; Höcker, H. Chemical Vapour Deposition Polymerization of Substituted [2.2]Paracyclophanes. *Macromol. Rapid Commun.* **1998**, *19*, 441−445.
(34) Hopf, H.; Zander, M.; Hermann, E. Phosphoreszenzeigen-schaften von Methyl-, Chlor-Und Brom-Derivaten Des [2.2] Para-cyclophans. *Z. Naturforsch., A: J. Phys. Sci.* **1987**, *42*, 1041−1042.
(35) Kim, Y. K.; Noh, J.; Nayani, K.; Abbott, N. L. *Soft Matter from Liquid Crystals*. Soft Matter 2019, *15*, 6913−6929. DOI: 10.1039/c9sm01424a.
(36) Hartono, D.; Bi, X.; Yang, K. L.; Yung, L. Y. L. An Air-Supported Liquid Crystal System for Real-Time and Label-Free Characterization of Phospholipases and Their Inhibitors. *Adv. Funct. Mater.* **2008**, *18*, 2938−2945.
(37) Nazarenko, V. G.; Pergamenshchik, V. M.; Koval'chuk, O. V.; Nych, A. B.; Lev, B. I. Non-Debye Screening of a Surface Charge and a Bulk-Ion-Controlled Anchoring Transition in a Nematic Liquid Crystal. *Phys. Rev. E: Stat. Phys., Plasmas, Fluids, Relat. Interdiscip. Top.* **1999**, *60*, 5580−5583.
(38) Popov, P.; Mann, E. K.; Jákli, A. Thermotropic Liquid Crystal Films for Biosensors and Beyond. *J. Mater. Chem. B* **2017**, *5*, 5061−5078.
(39) Lahann, J.; Höcker, H.; Langer, R. Synthesis of Amino[2.2]-Paracyclophanes - Beneficial Monomers for Bioactive Coating of Medical Implant Materials. *Angew. Chem., Int. Ed.* **2001**, *40*, 726−728.
(40) Deng, X.; Eyster, T. W.; Elkasabi, Y.; Lahann, J. Bio-Orthogonal Polymer Coatings for Co-Presentation of Biomolecules. *Macromol. Rapid Commun.* **2012**, *33*, 640−645.
(41) Chen, H. Y.; Hirtz, M.; Deng, X.; Laue, T.; Fuchs, H.; Lahann, J. Substrate-Independent Dip-Pen Nanolithography Based on Reactive Coatings. *J. Am. Chem. Soc.* **2010**, *132*, 18023−18025.
(42) Jiang, X.; Chen, H. Y.; Galvan, G.; Yoshida, M.; Lahann, J. Vapor-Based Initiator Coatings for Atom Transfer Radical Polymer-ization. *Adv. Funct. Mater.* **2008**, *18*, 27−35.
(43) Nandivada, H.; Chen, H. Y.; Lahann, J. Vapor-Based Synthesis of Poly[(4-Formyl-p-Xylylene)-Co-(p-Xylylene)] and Its Use for

Biomimetic Surface Modifications. *Macromol. Rapid Commun.* **2005**, *26*, 1794−1799.
(44) Popov, P.; Honaker, L. W.; Mirheydari, M.; Mann, E. K.; Jákli, A. Chiral Nematic Liquid Crystal Microlenses. *Sci. Rep.* **2017**, *7*, 1603.
(45) Cai, S.; Shi, H.; Tian, D.; Ma, H.; Cheng, Z.; Wu, Q.; Gu, M.; Huang, L.; An, Z.; Peng, Q.; Huang, W. Enhancing Ultralong Organic Phosphorescence by Effective π-Type Halogen Bonding. *Adv. Funct. Mater.* **2018**, *28*, No. 170504.
(46) Gustafson, T. P.; Lim, Y. H.; Flores, J. A.; Heo, G. S.; Zhang, F.; Zhang, S.; Samarajeewa, S.; Raymond, J. E.; Wooley, K. L. Holistic Assessment of Covalently Labeled Core-Shell Polymeric Nanoparticles with Fluorescent Contrast Agents for Theranostic Applications. *Langmuir* **2014**, *30*, 631−641.
(47) Ma, C.; Han, T.; Kang, M.; Liarou, E.; Wemyss, A. M.; Efstathiou, S.; Zhong Tang, B.; Haddleton, D. Aggregation-Induced Emission Active Polyacrylates via Cu-Mediated Reversible Deactivation Radical Polymerization with Bioimaging Applications. *ACS Macro Lett.* **2020**, *9*, 769.
(48) Ma, H.; Shi, W.; Ren, J.; Li, W.; Peng, Q.; Shuai, Z. Electrostatic Interaction-Induced Room-Temperature Phosphorescence in Pure Organic Molecules from QM/MM Calculations. *J. Phys. Chem. Lett.* **2016**, *7*, 2893−2898.
(49) Lim, E. C.; Yu, J. M. H. Vibronic Spin-Orbit Interactions in Heteroaromatic Molecules. II. Phosphorescence of Quinoxaline and Other Diazanaphthalenes. *J. Chem. Phys.* **1968**, *49*, 3878−3884.
(50) Zhang, L.; Wei, M.; Shao, L.; Li, M.; Dai, W.; Cui, Y.; Li, Z.; Zhang, C.; Wang, W. Enhanced Parylene-C Fluorescence as a Visual Marker for Neuronal Electrophysiology Applications. *Lab Chip* **2018**, *18*, 3539−3549.
(51) Gu, L.; Ye, W.; Liang, X.; Lv, A.; Ma, H.; Singh, M.; Jia, W.; Shen, Z.; Guo, Y.; Gao, Y.; Chen, H.; Wang, D.; Wu, Y.; Liu, J.; Wang, H.; Zheng, Y. X.; An, Z.; Huang, W.; Zhao, Y. Circularly Polarized Organic Room Temperature Phosphorescence from Amorphous Copolymers. *J. Am. Chem. Soc.* **2021**, *143*, 18527−18535.
(52) Gu, L.; Wu, H.; Ma, H.; Ye, W.; Jia, W.; Wang, H.; Chen, H.; Zhang, N.; Wang, D.; Qian, C.; An, Z.; Huang, W.; Zhao, Y. Color-Tunable Ultralong Organic Room Temperature Phosphorescence from a Multicomponent Copolymer. *Nat. Commun.* **2020**, *11*, 944.

https://doi.org/10.1021/acsapm.2c01477
ACS Appl. Polym. Mater. 2023, 5, 1670−1680